

# I-shaped thermally actuated VHF resonators with submicron components

H.J. Hall<sup>a,\*</sup>, A. Rahafrooz<sup>b</sup>, J.J. Brown<sup>a</sup>, V.M. Bright<sup>a</sup>, S. Pourkamali<sup>b</sup>

<sup>a</sup> Department of Mechanical Engineering, University of Colorado at Boulder, Boulder, CO 80309-0427, USA

<sup>b</sup> Department of Electrical and Computer Engineering, University of Denver, Denver, CO 80210, USA

## ARTICLE INFO

### Article history:

Received 14 April 2012

Received in revised form 6 December 2012

Accepted 10 December 2012

Available online 20 December 2012

### Keywords:

Resonator  
Thermal actuator  
Piezoresistive  
VHF

## ABSTRACT

Thermally actuated piezoresistive readout single crystal silicon (SCS) resonators with a device footprint of  $\sim 110 \mu\text{m}^2$  have been experimentally demonstrated at operating frequencies of 112–176 MHz. An SOIMEMS fabrication process was developed which incorporates electron beam lithography to achieve submicron dimensions. Demonstrated performance under vacuum (50–70 Torr) includes a  $Q=5750$  and motional conductance of  $89.6 \mu\text{A/V}$ . Frequency tunability of 2.1% in ambient and 3.66% under vacuum is achieved by variation of the DC bias current. The effects of asymmetry of the devices on operating frequency due to fabrication imperfections are considered qualitatively using commercial modeling software.

© 2012 Elsevier B.V. All rights reserved.

## 1. Introduction

The concept of thermally actuating high frequency resonators and utilizing piezoresistors to sense their motion has been around for a considerable amount of time [1,2] and continues to be used in designs today [3–5]. Operation of these devices is based upon modulation of local thermal gradients within the resonant structure to excite particular structural modes. This has been typically accomplished through localized Joule heating of resistors on the surface of the structure created by ion implantation. The approach is relatively simple in both fabrication and operation compared to traditional alternatives, which either require ceramic films (piezoelectrics) or nanoscale gap formation (capacitively driven and/or sensed devices).

Recently an alternative approach to thermal-piezoresistive resonant devices has been considered with the development of in-plane extensional mode resonators fabricated entirely by patterning a single layer of uniformly doped single-crystal silicon (SCS) [6–8]. The concept of operation is similar to the aforementioned devices except the localized regions in which the heating occurs are explicitly controlled through the geometry of the devices. In addition, for two-terminal operation, the piezoresistive readout is integrated into the device structure (i.e. no additional readout resistors are required). The merits to this approach are primarily two-fold: (1) the fabrication is simpler, as no additional patterning of resistors or doping is required, making aggressive size reduction possible and potential on-chip integration with electronics

easier; and (2) if the piezoresistive coefficient of the material is negative and its small signal voltage to current gain, or motional conductance, is sufficiently high an phenomenon known as self- $Q$  enhancement [9] can occur from internal positive feedback; this can allow device operation as a oscillator without the need for additional circuitry [10]. Thus there exists considerable potential for these devices in both sensing applications and on-chip RF electronics.

Previous work [6] has fabricated the I-shaped or dumbbell geometry (see Fig. 1) using a conventional SOIMEMS process and demonstrated frequencies up to 61 MHz with device footprints of  $350 \mu\text{m}^2$  or larger. While the performance of the previously reported devices was impressive ( $Q$  up to  $\sim 38,000$ ; motional conductance up to  $\sim 25 \text{ mA/V}$ ) lumped element theory predicts that the performance should improve dramatically as critical dimensions are scaled to smaller sizes for higher operating frequencies [6]. In addition, as these devices could be potentially applied toward on-chip RF signal processing, further miniaturization affords the possibilities of denser integration and continued reduction of the footprint of analog electronics and integrated circuits. The central motivation for this work was to examine this premise experimentally and develop an understanding of the effects of reducing dimensions on device performance. This paper presents the initial work toward this effort, expanding upon the results reported in [11], using I-shaped resonators with submicron feature sizes fabricated from a thin SOI device layer.

## 2. Device operation and performance metrics

The operation of the thermal-piezoresistive resonant devices in this work primarily results from the interaction of the mechanical, thermal, and electrical response of the center actuator arms

\* Corresponding author at: Department of Mechanical Engineering, University of Colorado - Boulder, 427 UCB, Boulder, CO 80309-0427, USA. Tel.: +1 3034927151.  
E-mail address: [Harris.Hall@colorado.edu](mailto:Harris.Hall@colorado.edu) (H.J. Hall).

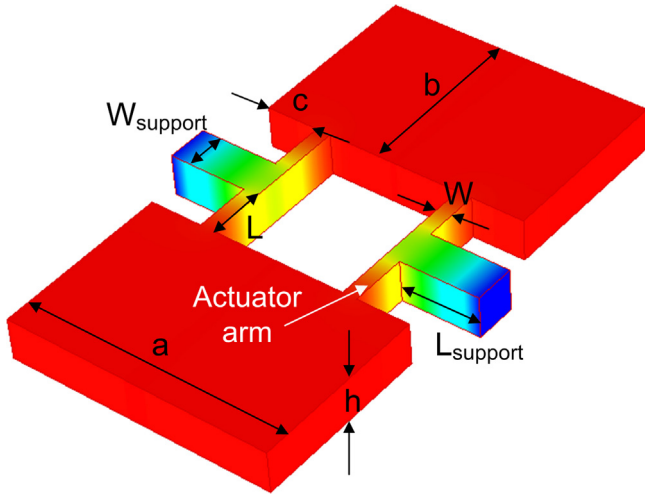


**Fig. 1.** Graphical schematic of I-shaped or dogbone resonator geometry with dimensions. Colors are indicative of an arbitrary steady state temperature distribution for DC applied voltage with the support anchor ends acting as heat sinks at a fixed temperature. The temperature gradient evident in the actuator arms (width =  $W$ , length =  $L$ ) is amplitude modulated by the addition of an AC drive voltage. (For interpretation of the references to color in this figure legend, the reader is referred to the web version of this article.)

in the structure (indicated in Fig. 1). Like all thermally actuated resonators, due to the square relationship between ohmic power loss and electrical voltage, a combination of AC signal and DC bias voltages is required for a frequency component of the cyclic Joule heating to match that of the applied AC signal. Excitation with AC voltage alone is possible, but the resonant mechanical response would occur at a frequency twice that of the input voltage. The alternating tensile and compressive stresses from thermal expansion and contraction of the actuator arms is sufficient to induce excitation, despite the cutoff frequency of the thermal response of the actuator typically being much less than the intrinsic mechanical frequency of the structure's longitudinal mode. When the material exhibits significant piezoresistivity, this expansion/contraction of the arms causes modulation of the DC current, leading to an AC current component called the motional current, which can be detected. In this geometry, because the longitudinal acoustic waves which propagate from the actuator arms are perpendicular to the support arm the amount of leakage through the support arms is reduced in comparison to geometries where the actuator also acts as a structural support to the substrate [7,8,12].

By considering the electrical, thermal, and mechanical subsystems, lumped systems analysis of the device dynamics [6], yields the small signal voltage to current gain, or motional conductance,  $g_m$ , to be:

$$g_m = 2\alpha E \pi_l Q \frac{I_{dc}^2}{C_{th} \omega_o} = 2\alpha E \pi_l \frac{I_{dc}^2}{C_{th} \Delta \omega} \quad (1)$$

where  $\alpha$  is the coefficient of thermal expansion,  $E$  is Young's modulus ( $130 \times 10^{11}$  Pa for (100) silicon),  $\pi_l$  is longitudinal piezoresistive coefficient modulus ( $\sim 50 \times 10^{-11}$  Pa $^{-1}$  for (100) silicon as suggested by [13]),  $Q$  is the quality factor,  $I_{dc}$  is the dc current,  $C_{th}$  is the thermal capacitance of a pair of actuator arms,  $\omega_o$  is the natural undamped mechanical resonant frequency, and  $\Delta \omega$  is the full width half maximum (FWHM) of the resonant peak. In this formulation the mechanical system is considered a classic driven harmonic oscillator (2nd order mass-spring-damper). The geometric dimensions and the elastic modulus of the material in turn define the natural mechanical resonant frequency of the extensional (or longitudinal) mode of the structure. The dampening inherent to the resonator is captured by either  $Q$  or FWHM. Optimum device

performance entails both maximizing the motional conductance and minimizing the power consumption. To capture both of these factors a figure of merit (FOM) which ratios the two is defined as

$$FOM = \frac{g_m}{P_{dc}} = \frac{2\alpha E \pi_l Q}{C_{th} \omega_o (R_A + R_S)} \quad (2)$$

where  $P_{dc}$  is the DC power,  $R_A$  is the resistance of the actuator arm, and  $R_S$  is the additional series resistance of the resonator. Per (1) and (2) if the device is scaled down by a factor  $S$ ,  $g_m$  increases by a square relationship (i.e.  $g_m$  is proportional to  $S^2$ ), and FOM increases linearly (i.e. FOM is proportional to  $S$ ).

The driving factor in the improvement with scaling lies with the thermal capacitance of the actuators' arms. A single pair of actuator arms can be considered to have an effective thermal capacitance,  $C_{th}$ , of

$$C_{th} = \beta C_{LE} = 2\beta \rho L W h c_H \quad (3)$$

where  $C_{LE}$  is the lumped-element thermal capacitance,  $\beta$  is a correction factor which has been established from finite-element analysis [14] to be between 1.02 and 1.11,  $\rho$  is the density ( $2.33 \times 10^{-15}$  kg/ $\mu\text{m}^3$  for silicon),  $W$  is the actuator width,  $L$  is the actuator length, and  $c_H$  is the specific heat of silicon ( $700 \text{ J kg}^{-1} \text{ K}^{-1}$ ). The factor of 2 is included because this capacitance represents a pair of individual actuators as defined in Fig. 1.

### 3. Device fabrication

The fabrication process, shown in Fig. 2, was adapted from previous work to accommodate electron beam lithography (EBL) and subsequent patterning of necessary submicron critical device dimensions. The starting wafer was silicon-on-insulator (SOI) with a 340 nm Si (100) device layer and 1  $\mu\text{m}$  thick buried oxide (BOX) layer on a conductive silicon substrate. Originally doped p-type with boron (14–22  $\Omega\text{-cm}$  per the manufacturer), the device layer was compensation doped to n-type with phosphorus. Device patterning was performed along the (100) direction to maximize the negative amplitude of the longitudinal piezoresistive coefficient,  $\pi_L$ . Resistivity of the device layer was measured by 4-point probe to be  $\sim 0.01 \Omega\text{ cm}$ . The two-terminal device interconnect pads (area  $\sim 145,000 \mu\text{m}^2$  each) and alignment markers were patterned from a thermally evaporated 100 nm Cr/25 nm Au metal stack using photolithography (S1813 photoresist) and lift-off. The metal pads were linked by a  $14 \mu\text{m} \times 20 \mu\text{m}$  rectangular bridge from which the devices were patterned. The Au layer was needed only to provide necessary visibility of the EBL alignment markers and was removed from a  $30 \mu\text{m}$  square area centered about the bridge using photolithography and wet etching (Transene TFA Au Etchant). Patterning of the device geometry was then performed using EBL (JEOL JSM-5910LV SEM with Nanoscale Pattern Generation System software) of PMMA and developed. The pattern was transferred to the Cr using a timed wet etch (Cyantek CR-7S). Reactive Ion Etching (RIE) was performed (5 sccm  $\text{SF}_6$ ; 15 sccm  $\text{CHF}_3$ , 150 W, 10 mTorr) to etch the device pattern into the silicon device layer. After the silicon etch the remaining Au and Cr were stripped in wet etchants and rinsed in deionized water. Since the BOX acts as an etch stop for this RIE chemistry, profilometry scans (Dektak 3030) were performed on the pads to check the device layer thickness after metal stripping. Device layer thickness was confirmed to be  $340 \pm 10 \text{ nm}$ . To complete fabrication, the devices were released in 48%  $\text{HF}_{(\text{aq})}$  (4 min etch time) followed by  $\text{CO}_2$  critical point drying (Fig. 3).

Close examination of the devices using scanning electron microscopy showed that the etching was anisotropic with  $\sim 15^\circ$  of outward slope. In addition, significant roughness along the edges and filleting of the corners was apparent. Seven measurements were performed across the top surface for each dimension of the

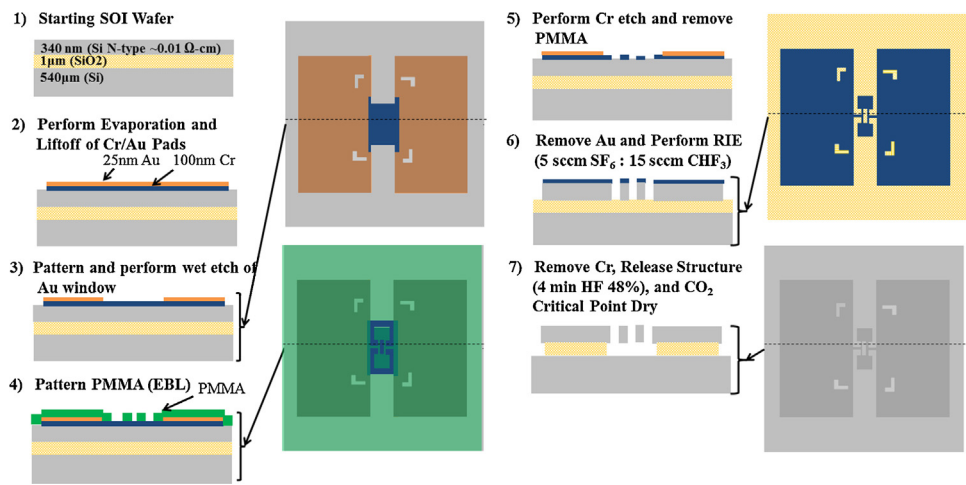


Fig. 2. Fabrication process.

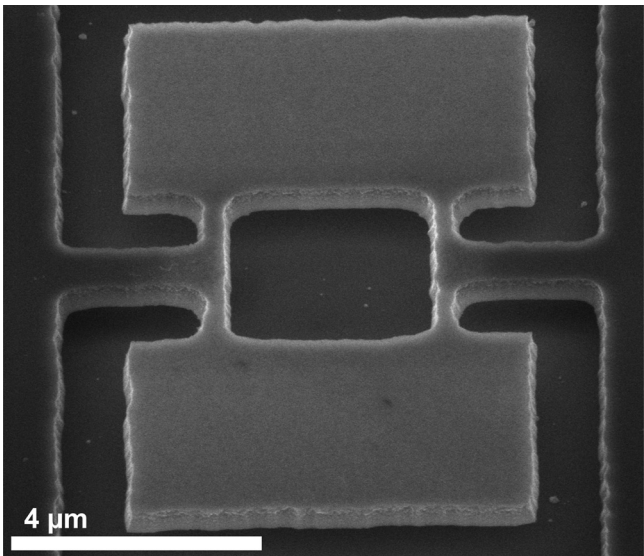


Fig. 3. SEM image (12,500×, 52° tilt) of suspended Device A.

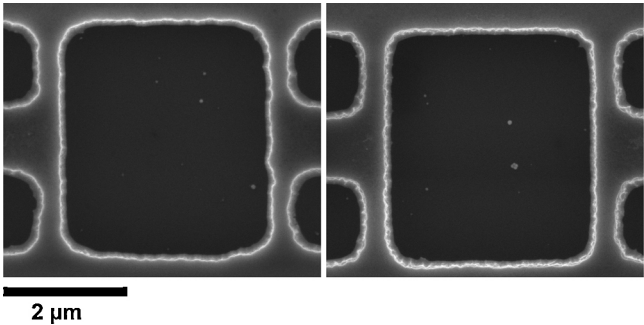


Fig. 4. SEM images (25,000×, top view) of the actuator arms for Device A (left) and Device B (right). The arm widths in Device A are noticeably asymmetric.

variation among the arms. Overall, Device B exhibited the best consistency of arm width and symmetry, while Device A was the worst. Fig. 4 shows images of each for comparison. The overall device footprint is  $\sim 110\text{ }\mu\text{m}^2$  excluding the bonding pads. The active area is  $\sim 70\text{ }\mu\text{m}^2$  [11].

4. Device characterization

Devices were individually wire bonded to a printed test circuit board, depicted by the schematic in Fig. 5, for examination of device resonant performance. A network analyzer (Agilent Technologies E5061B) provided the input AC voltage and recorded the transmission behavior ( $S_{21}$  parameter) of the signal through the circuit depicted. An additional DC source (Agilent E3647A) was used to provide the necessary bias current to power the device. The DC current was measured using a digital multimeter (Agilent 34405A). The substrate was grounded and additional resistive and capacitive components provided isolation of the sources as shown. Devices were examined in vacuum ( $\sim 50\text{--}70$  Torr) and ambient atmospheric conditions at different DC bias currents.

**Table 1**  
Average measured dimensions of devices as defined in Fig. 1. Measurement statistics are listed for the actuator arms as indicators of roughness and asymmetry present. Dimensions are (thickness  $h = 340\text{ nm}$ ).

Resonator dimensions ( $\mu\text{m}$ )									
Device	$a$ ( $n = 7$ )	$b$ ( $n = 7$ )	$c$ ( $n = 7$ )	$L$ ( $n = 7$ )	$W$ ( $n = 28$ )	$\% \sigma_W$ single arms	$\% \sigma_W$ between arms	$W_{\text{support}}$ ( $n = 7$ )	$L_{\text{support}}$ ( $n = 7$ )
A	6.47	4.40	1.24	1.35	0.32	5.24	9.06	1.03	2.37
B	6.49	4.45	1.24	1.41	0.35	4.05	2.44	1.00	2.42
C	6.51	4.43	1.14	1.27	0.44	3.93	8.46	1.13	2.18
D	6.70	4.72	1.13	1.00	0.80	4.76	6.81	1.38	1.88

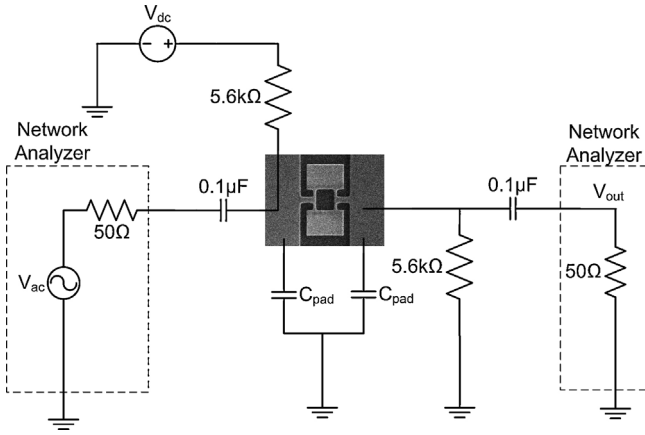


Fig. 5. Electrical test circuit schematic.

To determine the quality factor and motional conductance, post-measurement analysis was performed on the data to remove the effect of  $S_{21}$  feedthrough floor. The electrical equivalent model shown in Fig. 6 was used to extract the motional conductance values. The bias resistors were neglected as they are two orders of magnitude larger than the 50 Ω impedance of the network analyzer. The pad capacitance was also determined to be negligible at the operating frequencies in this work. This model is limited in that the parasitic series resistance for the devices, which is likely significant based on the device geometry, is not accounted for, making the values extracted from the measurements somewhat conservative. From this model, the ratio of the output voltage to the input voltage of the network analyzer at resonance can be determined to be

$$\frac{V_o}{V_s} = \frac{50 \Omega}{2(50 \Omega) + (1/(G_a + G_m))} \quad (4)$$

where  $G_a$  is the conductance of the device actuator, and  $G_m$  is the measured motional conductance. At frequencies distant from the resonant peak  $G_m$  is zero. By interpolating between the distant transmission regions adjacent to the device's resonant response the transmission "floor",  $T_{dbm \text{ floor}}$ , can be calculated. This value is effectively an estimate of the device's transmission with its resonant capabilities removed allowing  $G_a$  to be solved per Eq. (4)

$$G_a = \frac{-1}{(-(50 \Omega)/10^{T_{dbm \text{ floor}}/20}) + 2(50 \Omega)} \quad (5)$$

Likewise using (4) the  $G_m$  is

$$G_m = \frac{-1}{-((50 \Omega)/10^{T_{db}/20}) + 2(50 \Omega)} - G_a \quad (6)$$

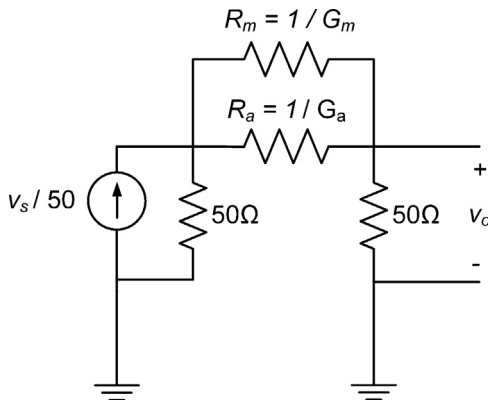
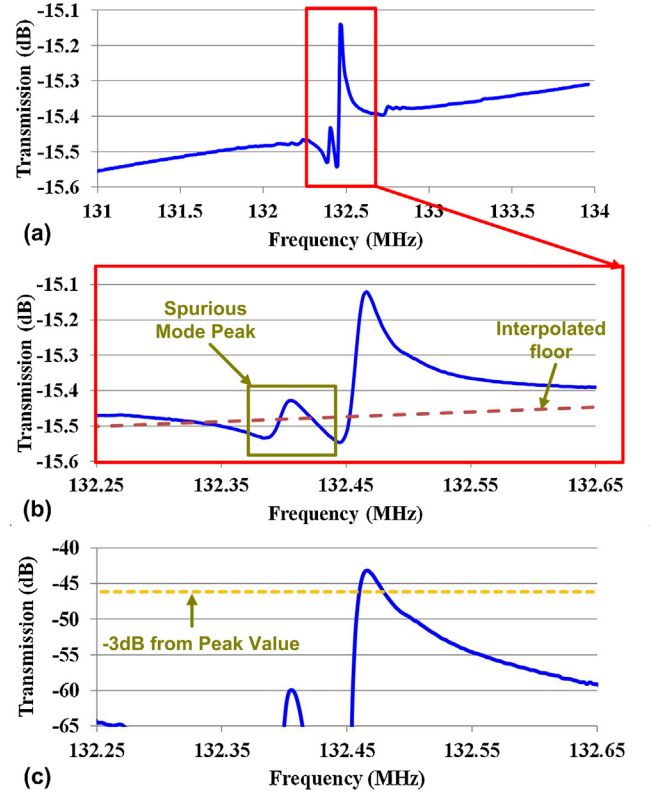
Fig. 6. Electrical equivalent circuit for measurement of  $G_m$ .

Fig. 7. Frequency responses of Device B under DC bias current of 1.3 mA (a) measured data directly from the network analyzer, (b) measured data in region of peak with interpolated feedthrough floor highlighting spurious mode and (c) feedthrough removed data used for measurement of  $Q$ .

where  $T_{dB}$  is the measured signal level in dB from the network analyzer at the resonant peak. Motional conductance was calculated for each device by applying the relations (4) and (5) at the device's resonant peak frequency (i.e.  $G_m @ \text{peak} = g_m$ ).

It can be shown that when both  $R_A$  and its parallel combination with  $R_M$  are much greater than the internal impedance of the network analyzer, which is a valid assumption for devices in this work, Eq. (6) simplifies to

$$G_m = \frac{1}{2(50 \Omega)} (10^{T_{dB}/20} - 10^{T_{db \text{ floor}}/20}) \quad (7)$$

The variation of  $G_m$  in the region of the resonant peak can thus be easily determined by (7) and, after converting back to dB, allows for direct measurement of  $Q$ . Fig. 7 illustrates this process showing measured data for Device B (Fig. 7a and b) with the same data after feedthrough removal (Fig. 7c) from which the  $Q$  value is extracted.

The measured performance results for each device are presented in Table 2. Overall the frequency of operation increased with shorter and wider actuator arms ranging from 112 MHz to 176 MHz. This is expected as the spring constant,  $k$ , for the longitudinal actuator can be approximated as  $k = WhE/L$ . Device D showed the strongest performance in terms of  $Q$ , motional conductance, FOM, and FOM normalized by  $Q$ , while Device A exhibited the poorest. These results suggest that the quality of fabrication is influential.

Although the performance of these devices is strong, their measured motional conductance values are as much as two orders of magnitude less than expected values given by Eq. (1). Because the measured  $Q$  and  $I_{dc}$  are inputs for this equation, the only sources for deviation in lie in the material properties and the thermal capacitance. Although the material constants which support Eq. (2) do change with temperature, doping concentration, and crystal



**Table 2**

Measured Device Performance. The data in bold corresponds to that depicted in Fig. 6. Shaded cells correspond to data obtained during device operation in vacuum pressure (50–70 Torr).

Device	Measured Parameters				Calculated Parameters		
	Current (mA)	$Q$ Factor	Freq. (MHz)	$g_m$ ( $\mu\text{A/V}$ )	Power (mW)	FOM ( $\times 10^{-3} \text{V}^{-2}$ )	FOM / $Q$ ( $\times 10^{-6} \text{V}^{-2}$ )
A	0.703	2250	111.98	1.72	1.49	1.23	0.55
	1.303	2420	109.30	11.5	7.68	1.55	0.64
	1.103	1390	111.40	3.13	4.01	0.81	0.58
	1.411	1150	109.35	5.51	9.71	0.69	0.60
B	0.224	4240	135.87	1.83	0.110	16.72	3.95
	<b>1.299</b>	<b>5750</b>	<b>132.46</b>	<b>89.6</b>	<b>6.77</b>	<b>13.23</b>	<b>2.30</b>
	0.801	1350	135.63	14.9	1.45	13.72	10.17
	1.51	690	131.85	22.9	9.17	4.13	5.99
C	0.403	1730	156.02	2.43	0.316	7.34	4.24
	1.442	3440	154.95	43.8	4.67	8.97	2.61
	1.509	780	154.87	18.9	4.96	3.65	4.68
	1.604	570	154.48	14.1	6.29	2.16	3.79
D	0.699	2270	170.97	2.63	1.02	2.36	1.04
	1.7	2620	166.94	22.0	9.37	2.16	0.82
	1.713	870	169.40	11.3	7.20	1.43	1.64
	1.803	860	166.99	12.6	11.5	1.01	1.171
= data obtained under vacuum pressure (50–70 torr)							

**Table 3**

Material parameters and settings used for modal analysis simulation.

Geometry (after Device B)		Relevant material parameters (isotropic)		Meshing
$h$	340 nm	Young's modulus, $E$	$1.3 \times 10^{11}$ Pa	- Ideal device (Fig. 9a): Manhattan brick parabolic elements (0.09 $\mu\text{m}$ , 0.09 $\mu\text{m}$ , 0.5 $\mu\text{m}$ ).
$a$	6.5 $\mu\text{m}$	Poisson's ratio, $\nu$	0.278	
$b$	4.3 $\mu\text{m}$	Density, $\rho$	$2.33 \times 10^{-15}$ kg/ $\mu\text{m}^3$	
$c$	1.2 $\mu\text{m}$	Internal Stress	0 MPa	
$L$	3.7 $\mu\text{m}$	<b>Boundary conditions</b>		- Non-ideal (e.g. Fig. 9b): tetrahedral mesh parabolic elements (0.175 $\mu\text{m}$ )
$W$	350 nm	Support ends fixed		
$W_{\text{support}}$	1 $\mu\text{m}$			

orientation, they are not expected to differ from their room temperature values by 2 orders of magnitude. One consideration is that additional mass may need to be considered beyond that of the actuator arms for the formulation of the effective thermal capacitance. The results reported in [6] include the portion of support arm mass between the actuator arms, however this alone does not compensate for the difference. One possibility is that larger portions of the support arms themselves may need to be considered in the calculation. Since Eq. (1) is formulated assuming perfect lateral and longitudinal symmetry of the device (i.e. the actuator arms all share the same frequency response), one possibility may be that asymmetry in the geometry is altering the shape of the resonant mode and thereby degrading the readout. Furthermore, the relative difference in the temperature gradients of the actuator arms from the asymmetry may not be as efficient in exciting this altered mode shape. Thus, the quality of fabrication may degrade the estimation of motional conductance provided by Eq. (1), beyond effects inherent to degradation of the  $Q$ .

It is difficult to estimate the quantitative effect that filleting, edge roughness, and asymmetry in the actuator arms may have on the performance metrics, however aberrations in the spectral response suggest that the mode shape is non-ideal. The measured frequency response for Device B, shown in Fig. 7b, clearly shows the presence of a spurious mode near the resonant peak, possibly due to device asymmetry.

For qualitative comparison of the effects of fabrication imperfections on the longitudinal mode of the device structure, a modal analysis series was performed using Coventorware's MemMech utility based upon the measured dimensions of Device B. Parameters for the simulation are listed in Table 3. The series included the stated geometry with square features (the ideal device shown

in Fig. 8a), filleting corners (500 nm radius), filleting corners and 15° sidewalls, and finally filleting corners with 15° sidewalls and asymmetric arms widths as the measured averages of Device B (shown in Fig. 8b). The results are summarized in Table 4. The frequency difference from the model shown in Fig. 8b and that measured by Device B (~20 MHz) is likely due to differences in the

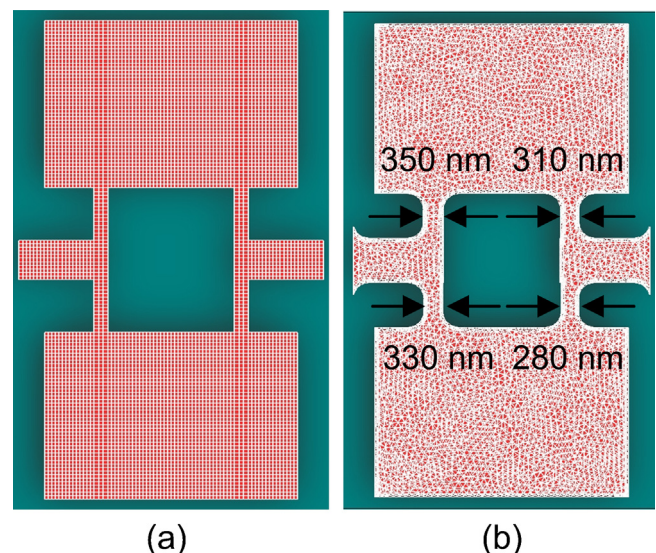


**Fig. 8.** Meshed solid models of Device B (a) is ideal geometry with square features (b) incorporates filleting with a 500 nm radius, 15° sidewalls and asymmetric actuator arm widths.

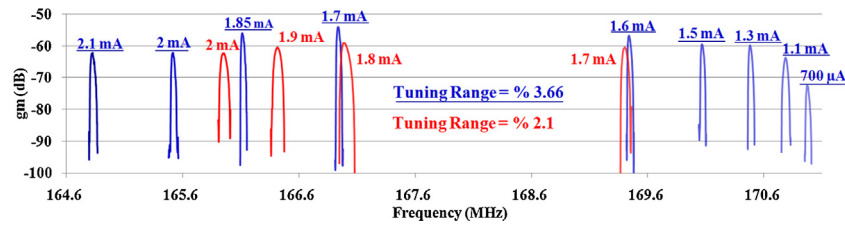


**Fig. 9.** Measured frequency responses for Device D with different bias currents. Red and blue (underlined) plots refer to air and vacuum testing conditions, respectively. (For interpretation of the references to color in this figure legend, the reader is referred to the web version of this article.)

**Table 4**

Modal frequencies from MemMech for different geometry variations.

Geometry variation	Longitudinal modal frequency
Ideal (square)	138.6 MHz
Filleting corners (500 nm radius)	151.4 MHz
Filleting corners and 15° sidewalls	162.1 MHz
Asymmetric actuator arm widths with filleting corners and 15° sidewalls	158.4 MHz

actual material parameters under operating conditions. The data in Table 3 indicates that relatively minor variations in fabrication can play a significant role in the frequency of the resonant mode. In addition, it should be noted that the introduction of asymmetry also changes the mode shape introducing some lateral motion into the resonator proof masses. Videos of the simulated modal response for Fig. 8a (video S1) and b (video S2) are available as Supplementary Content. As previously discussed this altered mode may degrade the overall motional conductance of the device.

Similar to the previously reported larger scale devices [6], it was also observed that adjustment of the DC bias current allowed direct tuning of the operating frequency. The bias current was found to be inversely related to the operating frequency. A likely mechanism is that this effect results from the temperature-dependent softening of the elastic modulus [15]. Fig. 9 shows the measured frequency response for the motional conductance of the 170 MHz resonator at different DC bias currents, demonstrating frequency tuning capability of up to 2.1% in ambient and 3.66% in vacuum.

The performance of the devices was not entirely invariant throughout the tuning range of these devices. Fig. 10 shows a scatter plot of the  $Q$  normalized with frequency (or  $1/FWHM$ ) vs. the ratio of DC power to total actuator volume, which serves as a gross

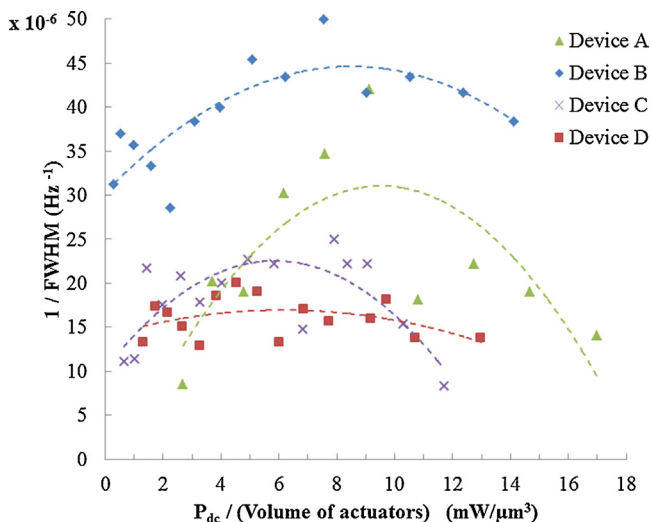


**Fig. 10.** Plot of  $1/FWHM$  vs. "power density" of actuators for each of the four devices. Second order polynomial fit curves are presented for reference.

measure of the power density within the actuators. This portrayal of performance allows easy comparison of devices with different operating frequencies and DC currents. Second-order polynomial fit lines are shown to indicate that there tends to be an optimum operating condition for each device. The optimums for these devices fall in the range of 6–12 mW/μm<sup>3</sup>. The initial increase in the  $1/FWHM$  with power density is likely an artifact of the signal rising above the feedthrough floor allowing better perceived  $Q$ . The drop in  $1/FWHM$  at higher power densities is likely due to the degradation in  $Q$  from the elevated temperature of the material.

## 5. Conclusions

This work demonstrated the highest frequency (112–176 MHz) and smallest footprint ( $\sim 110 \mu\text{m}^2$ ) thermal-piezoresistive single crystal silicon (SCS) resonators yet reported, offering increased promise for VHF signal processing applications. Device performance was strong, but expectations with reduced scaling as proposed in [6] were not met, suggesting there are limits to the practical applicability of the theory supporting Eq. (2). However, imperfections in the device patterning offer the possibility for further improvement. To this end, improvements are being pursued to the fabrication process in order to yield sharper, better defined features. Developing these devices as on-chip VHF oscillators is of primary interest for near-term applications. Variations to the device dimensions are being pursued in conjunction with 3D modeling to explore the optimum conditions for self- $Q$  enhancement at these higher frequencies. Methods to reduce the feedthrough floor for the readout are also being explored.

## Acknowledgements

This research was in part supported by the National Science Foundation (Award Number 1056068) and the Defense Advanced Research Projects Agency (DARPA) Center on Nanoscale Science and Technology for Integrated Micro/Nano-Electromechanical Transducers (iMINT), N/MEMS S&T Fundamentals program under Grant No. N66001-10-1-4007 issued by the Space and Naval Warfare Systems Center Pacific (SPAWAR). Fabrication was conducted in part at the Colorado Nanofabrication Laboratory a member of the NNIN sponsored by the National Science Foundation under Grant No. ECS-0335765. SEM imaging was performed at the University of Colorado at Boulder's Nanomaterials Characterization Facility. H. Hall also acknowledges the SMART Scholarship Program for financial support throughout the course of this work.

## Appendix A. Supplementary data

Supplementary data associated with this article can be found, in the online version, at <http://dx.doi.org/10.1016/j.sna.2012.12.006>.

## References

- [1] R.J. Wilfinger, P.H. Bardell, D.S. Chhabra, The resonator: a frequency selective device utilizing the mechanical resonance of a silicon substrate, IBM Journal 3 (1968) 113–118.

- [2] M.B. Othman, A. Brunnschweiler, Electrothermally excited silicon beam mechanical resonators, *Electronics Letters* 23 (1987) 728–730.
- [3] J.H. Seo, O. Brand, High Q-factor in-plane-mode resonant microsensor platform for gaseous/liquid environment, *Journal of Microelectromechanical Systems* 17 (2008) 483–493.
- [4] L. Beardslee, K. Demirci, Y. Luzinova, J. Su, B. Mizaikoff, S. Heinrich, F. Josse, O. Brand, In-plane mode resonant cantilevers as liquid phase chemical sensors with ppb range limits of detection, in: *Solid-State Sensors, Actuators, and Microsystems Workshop*, Hilton Head Island, SC, Transducers Research Foundation, 2010, pp. 23–26.
- [5] L.A. Beardslee, J. Lehmann, C. Carron, J. Su, F. Josse, I. Dufour, O. Brand, Thermally actuated silicon tuning fork resonators for sensing applications in air, in: *2012 IEEE 25th International Conference on Micro Electro Mechanical Systems (MEMS)*, IEEE Press, Paris, France, 2012, pp. 607–610.
- [6] A. Rahafrrooz, S. Pourkamali, High-frequency thermally actuated electromechanical resonators with piezoresistive readout, *IEEE Transactions on Electronic Devices* 58 (2011) 1205–1214.
- [7] A. Rahafrrooz, S. Pourkamali, Characterization of rotational mode disk resonator quality factors in liquid, in: *2011 Joint Conference of the IEEE International Frequency Control and the European Frequency and Time Forum (FCS) Proceedings*, IEEE Press, San Francisco, CA, 2011, pp. 1–5.
- [8] A. Hajjam, J.C. Wilson, A. Rahafrrooz, S. Pourkamali, Fabrication and characterization of thermally actuated micromechanical resonators for airborne particle mass sensing: II. Device fabrication and characterization, *Journal of Micromechanics and Microengineering* 20 (2010) 125019.
- [9] A. Rahafrrooz, S. Pourkamali, Active self-Q-enhancement in high frequency thermally actuated M/NEMS resonators, in: *2011 IEEE 24th International Conference on Micro Electro Mechanical Systems (MEMS)*, IEEE Press, Cancun, Mexico, 2011, pp. 760–763.
- [10] A. Rahafrrooz, S. Pourkamali, Fully micromechanical piezo-thermal oscillators, in: *Int. Electron Devices Meeting (IEDM)*, IEEE Press, San Francisco, CA, 2010, pp. 158–161.
- [11] H.J. Hall, A. Rahafrrooz, J.J. Brown, V.M. Bright, S. Pourkamali, Thermally actuated I-shaped electromechanical VHF resonators, in: *IEEE 25th International Conference on Micro Electro Mechanical Systems*, IEEE Press, Paris, France, 2012, pp. 737–740.
- [12] P.G. Steeneken, K. Le Phan, M.J. Goossens, G.E.J. Koops, G.J.A.M. Brom, C. van der Avoort, J.T.M. van Beek, Piezoresistive heat engine and refrigerator, *Nature Physics* 7 (2011) 354–359.
- [13] C.-H. Cho, R.C. Jaeger, J.C. Suhling, Characterization of the piezoresistive coefficients of (1 0 0) silicon from –150 to +125°C, in: *Proceedings of IPACK2007 ASME InterPACK'07*, ASME, Vancouver, British Columbia, Canada, 2007, pp. 1–14.
- [14] A. Rahafrrooz, S. Pourkamali, Fabrication and characterization of thermally actuated micromechanical resonators for airborne particle mass sensing: I. Resonator design and modeling, *Journal of Micromechanics and Microengineering* 20 (2010) 125018.
- [15] J. Jeong, S. Chung, S.H. Lee, D. Kwon, Evaluation of elastic properties and temperature effects in Si thin films using an electrostatic microresonator, *Journal of Microelectromechanical Systems* 12 (2003) 524–530.

## Biographies

**Harris J. Hall** is currently working toward his Ph.D. in Mechanical Engineering at the University of Colorado at Boulder, researching mechanical MEMS/NEMS switches and thermal-piezoresistive resonators. He earned his B.S. in Electrical Engineering from Rensselaer Polytechnic Institute (1999), and an M.S. in Electrical Engineering from the Air Force Institute of Technology (2001). He was an active duty USAF officer for nearly 10 years prior to being awarded a 2009 DoD SMART scholarship to conduct his doctoral studies.

**Amir Rahafrrooz** received the B.Sc. degree in biomedical engineering from Isfahan University, Isfahan, Iran, in 2004, and the M.Sc. degree in bioelectric from Amirkabir University of Technology, Tehran, Iran, in 2007. Then he came to U.S. and started

his Ph.D. in the Department of Electrical and Computer Engineering, University of Denver under supervision of Prof. Siavash Pourkamali. His research interests were mainly related to RF MEMS. In 2009, he received the best research assistant award at Department of Electrical and Computer Engineering, University of Denver. He is also the 2009–10 recipient of the graduate studies fellowship for inclusive excellence and the 2010–11 recipient of the graduate studies dissertation fellowship. He was also nominated for the Best Student Paper Award in IEEE International Electron Devices Meeting 2010. He received his Ph.D. degree in August 2011. He is currently an Associate Research Scientist with the Department of Electrical and Computer Engineering, University of Denver, Denver, CO. His main research interests are in the areas of RF-MEMS with focus on high frequency thermal-piezoresistive micromechanical resonators/oscillators, resonant mass sensors and micro/nano fabrication technologies

**Joseph J. Brown** received an A.B. in Engineering Sciences from Dartmouth College, Hanover, NH, in 2000. He received the M.S. and Ph.D. degrees in Mechanical Engineering from the University of Colorado at Boulder in 2008 and 2010, respectively. He was recipient of a 2007 NSF Graduate Research Fellowship. He is presently a Research Associate at the University of Colorado Department of Mechanical Engineering. In 2004, he helped found carbon nanotube manufacturer NanoComp Technologies, Inc., of Concord, NH, and served there as Senior Engineer until 2006. His research interests center on precision assembly, mechanical characterization, applications of nanostructures and nanoscale systems, and the interface of materials technologies and MEMS design. He has published five refereed journal papers and three conference papers, and he is an inventor on three U.S. patents.

**Victor M. Bright** received a BSEE degree from the University of Colorado at Denver in 1986, and the M.S. and Ph.D. degrees from the Georgia Institute of Technology, in 1989 and 1992, respectively. He is the Alvah and Harriet Hovlid Professor and Chair of the Department of Mechanical Engineering, and the Faculty Director for Discovery Learning, College of Engineering and Applied Science (CEAS), University of Colorado at Boulder (UCB). From 2005 through 2007, he served as the Associate Dean for Research, CEAS, UCB. Prior to joining the University of Colorado, he was a Professor in the Department of Electrical and Computer Engineering, Air Force Institute of Technology, Wright-Patterson Air Force Base, OH (1992–1997). During 2004 he was a Visiting Professor at the Swiss Federal Institute of Technology (ETH–Zürich), Switzerland. His research activities include micro- and nano-electro-mechanical systems (MEMS and NEMS), silicon micromachining, microsensors/microactuators, optical, magnetic and RF microsystems, atomic-layer deposited materials, ceramic MEMS, MEMS reliability, and MEMS packaging. He is a Fellow of ASME, a Senior Member of IEEE, and an author of over 90 archived journal papers in the fields of MEMS, NEMS and microsystems. He has served on the Executive Committee of the ASME MEMS Division, on the Technical Program Committee of the IEEE MEMS 2000–2006 conferences, and as the General Co-Chair for the IEEE MEMS 2005 International Conference. He also served on the Technical Program Committees for the Transducers'03, Transducers'07, IEEE/LEOS Optical MEMS 2003–2005, and Hilton Head 2008 Solid-State Sensors and Actuators Workshop. He taught a Short Course on MEMS Packaging at Transducers'03 and Transducers'05.

**Siavash Pourkamali** (S'02–M'06) received the B.S. degree in electrical engineering from Sharif University of Technology, Tehran, Iran, in 2001, and the M.S. and Ph.D. degrees in electrical engineering from Georgia Institute of Technology, Atlanta, in 2004 and 2006, respectively.

He is currently an Assistant Professor in the Department of Electrical and Computer Engineering, University of Denver, Denver, CO. He is the holder of several issued patents and pending patent applications in the areas of silicon micro/nanomechanical resonators and filters and nanofabrication technologies, some of which have been licensed to major players in the semiconductor industry. His main research interests include the areas of integrated silicon-based MEMS and microsystems, micromachining technologies, RF MEMS resonators and filters, and nanomechanical resonant sensors. He is a recipient of a 2011 National Science Foundation CAREER Award, the 2008 University of Denver Best Junior Scholar Award, and the 2006 Georgia Tech Electrical and Computer Engineering Research Excellence Award. He was also a silver medallist in the 29th International Chemistry Olympiad (IChO) in 1997.